Experimental study on the development mechanism of short pitch corrugation using a downscale V-Track test rig

Zhang, Pan; Li, Zili

DOI
10.1016/j.triboint.2023.108293

Publication date
2023

Document Version
Final published version

Published in
Tribology International

Tribology International 180 (2023) 108293

Contents lists available at ScienceDirect

Tribology International

journal homepage: www.elsevier.com/locate/triboint

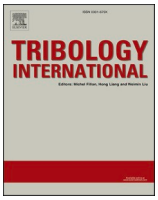

Experimental study on the development mechanism of short pitch corrugation using a downscale V-Track test rig

Pan Zhang, Zili Li *

Delft University of Technology, Section of Railway Engineering, Stevinweg 1, 2628 CN Delft, the Netherlands

ARTICLE INFO

Keywords:
Short pitch corrugation
V-Track test rig
Wheel-rail dynamic contact forces
Rail vibration modes

ABSTRACT

This paper presents an experimental study on the development mechanism of short pitch corrugation using an innovative downscale V-Track test rig. Rail corrugation is reproduced in the V-Track with two wavelengths of 6.4 mm and 8.9 mm. Based on the measured wheel-rail contact forces, track dynamic behaviors, and observations, the consistent development mechanisms of short pitch corrugation are identified. It is found the longitudinal mode at 574 Hz and the induced longitudinal dynamic force are dominant for corrugation formation at the major wavelength of 6.4 mm. This paper provides the first experimental evidence indicating that rail longitudinal vibration mode and its induced longitudinal force contribute to the consistent development of short pitch corrugation.

1. Introduction

Short pitch corrugation (hereinafter corrugation) is recognized as the periodic undulation of rail running surfaces on the tangent track with a wavelength range of 20–80 mm [1]. Fig. 1a shows a typical example of corrugation in the Dutch railway. Rail corrugation excites large wheel-rail impact forces, causes excessive vibration and noise, and accelerates the deterioration of the vehicle-track system, which considerably increases maintenance costs. Therefore, it is of great significance to identify the corrugation formation mechanism and develop effective root-cause solutions.

Many theoretical and numerical studies [2–11] have been performed to understand the corrugation development mechanism. S. L. Grassie and J. Kalousek [1] presented a feedback loop for a general corrugation mechanism, which comprises two features: the wavelength-fixing mechanism and the damage mechanism. Typical damage mechanism of short pitch corrugation are differential wear and plastic deformation [1,12–14], while different hypotheses have been proposed for the wavelength-fixing mechanism. The vertical pinned-pinned resonance was reported as the wavelength-fixing mechanism in [3,4,13], which is a rail vertical bending mode with a wavelength of two sleeper spans. S. Muller [7] introduced a geometrical filter function that allows corrugation development within a fixed wavelength band (i.e., 20–100 mm) and showed that both the vertical and lateral track dynamics in this band dominate corrugation development. Wu and Thompson [9] considered multiple wheel/rail interactions and found that wavelengths of short pitch corrugation are associated with several vertical vibration frequencies due to the wave reflections between the wheels, rather than the only pinned-pinned frequency in the case of a single wheel/rail interaction. Employing a three-dimensional (3D) finite element (FE) vehicle-track interaction model to study corrugation, Li et al. [6,15] indicated that rail longitudinal vibration modes are dominant for the corrugation initiation and that a consistency condition between the longitudinal and vertical vibration modes is likely to determine the corrugation growth. Based on this mechanism, Zhang et al. [16] designed a new rail constraint that can effectively mitigate corrugation.

Experimental studies have been conducted in the laboratory to validate and better understand the corrugation formation mechanism [17–21]. Bellette et al. [17] validated a tangent track corrugation model in terms of corrugation growth rate with a downscale two disk test rig. They also analyzed the effect of the speed variation and the friction modifier on corrugation growth and found that these two factors can considerably reduce the corrugation growth rate. Jin and Wen [19] reproduced rail corrugation with different wavelengths using a full-scale test rig. It was found that the high-frequency vibration of the test rig can initiate a corrugation on the smooth contact surfaces of the wheel under specific test conditions, including the non-zero steady creepage of the wheelset/rollers and the circumference of the wheel rolling circle approximately equal to a multiple of the corrugation wavelength. The majority of test facilities mainly concentrate on the simulation of the

* Corresponding author.
E-mail address: z.li@tudelft.nl (Z. Li).

https://doi.org/10.1016/j.triboint.2023.108293
Received 27 July 2022; Received in revised form 11 January 2023; Accepted 23 January 2023
Available online 25 January 2023

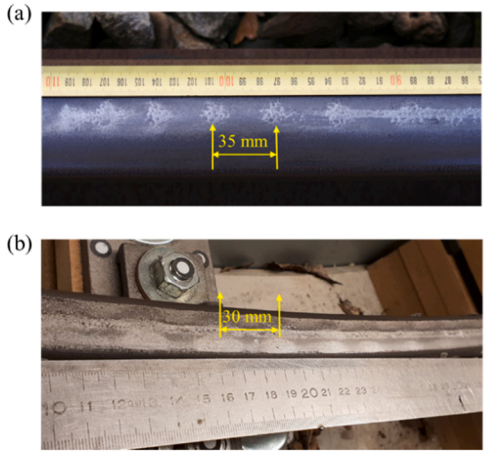

Fig. 1. Corrugation observed in the Dutch railway and reproduced in the V-Track test rig. (a) Corrugation with a wavelength of approximately 35 mm, Steenwijk, the Netherlands. (b) Corrugation with a wavelength of approximately 30 mm reproduced in the V-Track test rig after about 8000 rotations.

wheel-rail contact of the vehicle-track interaction. Little consideration has been taken into reproducing the dynamic behaviors of the vehicle-track system, especially in the high-frequency range, which is crucial to the wavelength-fixing of corrugation in the field [1]. Therefore, although the natural vibration modes of these test facilities can well explain the wavelengths of the reproduced corrugation [19,21], they may not be comparable to those of the real vehicle-track system because of the dynamic dissimilarity, and thus cannot be used to understand the wavelength-fixing mechanism of short pitch corrugation in the field.

To remedy the lack of dynamic similarity between the laboratory facilities and the real-life railways, an innovative downscale test rig called 'V-Track' has been developed by M. Naeimi et al. [18] to simulate vehicle-track dynamic interactions. The V-Track can comprehensively simulate both the wheel-rail contact and the high-frequency dynamic behaviors of the real vehicle-track system by the detailed treatment of wheel/rail material and geometry and the inclusion of important track structural components, such as fastenings, sleepers, and ballast layer. Therefore, it is suitable to perform wheel-rail contact experiments under highly dynamic loadings, such as short pitch corrugation, squats, and wheel polygonization. Fig. 1b shows an example of a reproduced corrugation in one of the configurations of the V-Track. Controlling the loading conditions of the V-Track and key measurement data, such as wheel-rail dynamic contact forces, are essential to reproduce and understand the corrugation formation mechanism experimentally. Zhang et al. [19] developed a force measurement system called "dynamometer" in the V-Track, which can measure the wheel-rail contact forces in the vertical, longitudinal, and lateral directions.

The present paper uses the innovative V-Track to reproduce rail corrugation and provide experimental evidence regarding wheel-rail contact forces, track dynamic behaviors, and hardness to understand its formation mechanism. The paper is organized as follows. Section 2 introduces the structure of the V-Track and the procedures to reproduce the rail corrugation. Section 3 presents the features of the reproduced corrugation in the V-Track in terms of spatial distribution, wavelength components, and hardness variation. Section 4 identifies the corrugation formation mechanism by analyzing the measured wheel-rail dynamic contact forces and track dynamic behaviors. Section 5 further discusses the experimental results and simulation results from the literature. The conclusions are drawn in Section 6.

2. Corrugation experiment in the V-Track

2.1. Experimental setup

The V-Track test rig consists of a maximum of four-wheel assemblies running over a ring track system. Two-wheel assemblies, wheel 1 (W1) and wheel 3 (W3), were utilized in the current configuration (see Fig. 2a). Figs. 2b and c show the structure and main components of W3. Cylindrical wheels (see "1" in Fig. 2c) with a radius of 65 mm were used. The wheels were obtained from an actual wheel rim to ensure the identical material as in the real field. W3 was connected to a guiding block ("3" in Fig. 2c) through an axle box ("2" in Fig. 2c). The wheel position is adjustable along the wheel axle. The guiding block, axle box, and wheel can move along two parallel guiding shafts ("9" in Fig. 2c) vertically under the preload of two primary suspension springs ("4" in Fig. 2c). The stiffness of each spring is 115 N/mm. The upper ends of these two springs were loaded by two nuts ("6" in Fig. 2c) through load cells ("5" in Fig. 2c). The spring load is adjustable in the range of 0–7500 N by screwing the nuts upward or downward along the threaded part of the guiding shafts. The angle of attack (AoA) of the wheel is adjustable between -2° and $+2^\circ$ by rotating the axle box around its vertical axis. The two-wheel assemblies were mounted on the arms of a steel frame ("7" in Fig. 2c), as shown in Fig. 2a. The steel frame was driven by a motor called 'driving motor' so that the wheel assemblies were pulled to run along the ring track. The maximum running speed is 40 km/h. Another motor, called 'braking motor,' was directly connected to the wheels through the braking shafts ("8" in Fig. 2c), which can apply a controllable negative/positive torque to the wheels to generate desired braking/traction forces.

The ring track has a radius of 2 m. This radius is not geometrically representative of any typical curvatures in real tracks. The lateral vehicle-track interaction, especially the lateral wheel-rail contact of different curvatures, can be simulated and investigated in the V-Track by adequately adjusting the AoA, the wheel conicity, as well as the rail inclination. The ring track comprised four sections of S7 rails [22] with a head curvature radius of 120 mm, connected through four rail joints. The rails were supported by railpads and were fixed on steel sleepers by clamps, as shown in Fig. 2d. In total, 100 sleepers were used, and the sleeper spacing was approximately 0.125 m. All sleepers were numbered from 1 to 100 for positioning; for instance, SL1 designates sleeper 1. Clamps were installed every three or four sleepers to simulate the fastening degradation, which may provide a preferred condition for corrugation initiation and growth [6]. In total the ring rails are constrained by fastening clamps on 25 sleepers. Underneath the sleepers were rubber pads used to reproduce the elasticity and damping of ballast layers in real tracks. Plywood layers simulated the subgrade. The rail inclination is adjustable between 0 and 1/10 by mounting wedges on plywood layers. In the experimental setup considered in this paper, the rail inclination was approximately zero to achieve the wheel-rail head contact. Overall, the inclusion of main track components in the V-Track makes it a suitable laboratory representation of the real-life vehicle--track system in high-frequency dynamic behaviors [23], which affects the corrugation wavelength.

The parameters of the V-Track test rig are designed to be approximately 1/5 scale of the real vehicle-track system based on the similarity law [23,24], as listed in Table 1. A more detailed description of the V-Track can be found in [22,23].

2.2. Corrugation experiment

Before the corrugation experiment, the loading conditions of the V-Track need first to be designed and adjusted to simulate the vehicle-track interaction on the field tangent track. The vertical (normal) load was adjusted to be around 4500 N to achieve maximum contact pressure of approximately 1.15 Gpa, similar to that in the field. The AoA was set to be as small as possible to simulate the wheel-rail lateral interaction on

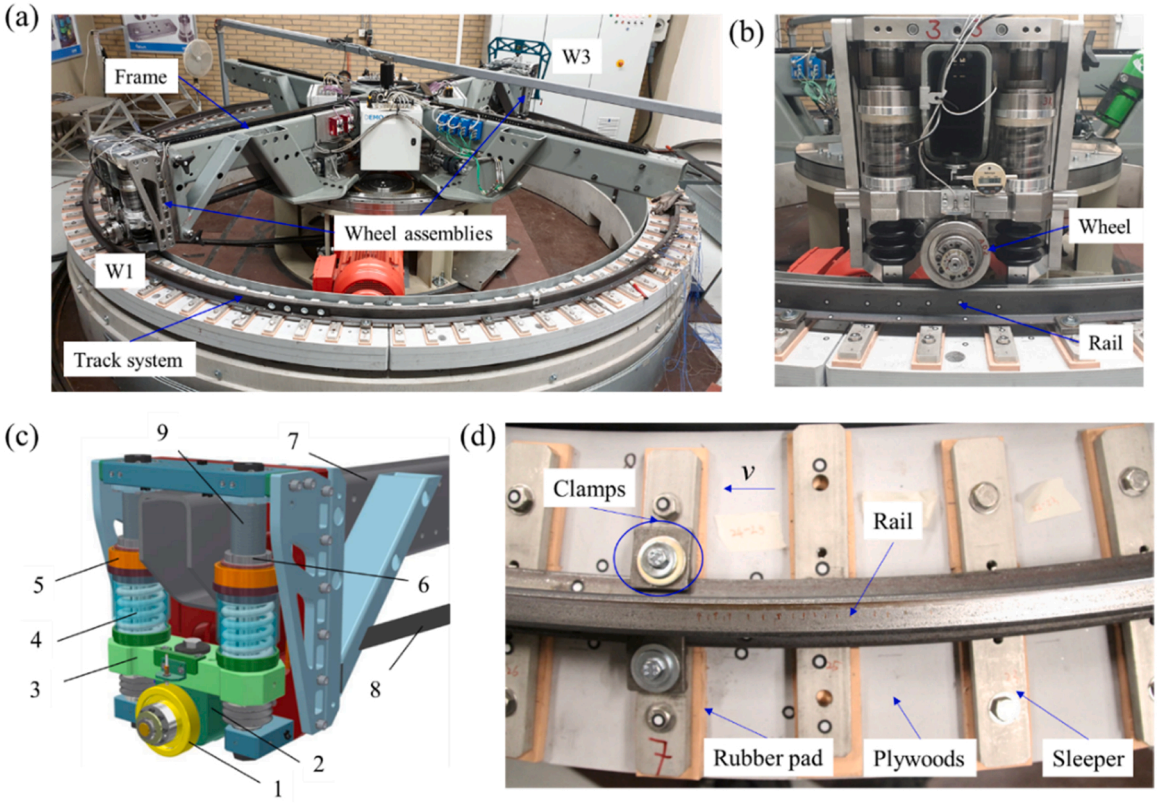

Fig. 2. The V-Track test rig for corrugation experiments. (a) The V-Track test rig in two-wheels assemblies configuration in the laboratory; (b) wheel 3 of the V-Track; (c) schematic drawing of components of W3 in CAD, 1) wheel, 2) axle box, 3) guiding block, 4) primary suspension springs, 5) load cells, 6) preload nut, 7) steel frame, 8) braking shaft, and 9) guiding shaft; (d) main components of the track system.

Table 1
Values of parameters of the V-Track test rig.

Components	Parameters	Values
Wheel, rail, sleeper material	Young's modulus	210 GPa
	Poisson's ratio	0.3
	Density	7800 kg/m^3
Wheel	Radius	65 mm
	Conicity	0
	Hardness	250 HB
Rail	Head curvature radius	120 mm
	Inclination	0
	Hardness	210 HB
Sleeper	Dimensions	255 × 40 × 15 mm
	Distance	125 mm
Primary suspension	Stiffness	230 kN/m
	Damping	100 N.s/m
Railpads	Stiffness	200 MN/m
	Damping	1.9 kN.s/m
Rubber pads to simulate ballast	Stiffness	10 MN/m
	Damping	0.86 kN.s/m

tangent tracks. The braking motor adjusted the wheel torque to achieve a relatively small adhesion coefficient between 0.05 and 0.15 because corrugation seems more reliably formed in low creep conditions [17]. The coefficient of friction was about 0.35 after cleaning and drying the rail and the wheel surfaces [25]. The running speed was 13 km/h. During the corrugation experiment, the wheel-rail contact forces were continuously measured and recorded by the dynamometer. Every 500 rotations, the V-Track was stopped for a visual inspection of the rail and wheel surfaces to check whether corrugation occurred or not. After the corrugation in the V-Track was reproduced, a 3D HandyScan test was performed to measure the spatial distribution of corrugation. A hardness test was then conducted to identify the hardness variation along the corrugation. Additionally, a hammer test was performed to obtain the dynamic behavior of the track, which is related to the corrugation characteristic frequencies and wavelengths. A detailed introduction of the wheel-rail contact force measurement, the 3D HandyScan test, the hardness test, and the hammer test is provided in the following sections.

2.2.1. *Wheel-rail contact force measurement*

A dynamometer has been developed in the V-Track to measure the wheel-rail contact forces in the vertical (z), longitudinal (rolling, x), and lateral directions (y) [22]. It consists of four 3-component piezoelectric force sensors mounted between the wheel assembly and the steel frame. The sampling frequency is 16.67 kHz. Fig. 3 shows the measured wheel-rail contact forces of W1 and W3 in three directions after adjusting the spring preload, the wheel torque, and the AoA based on the designed loading conditions. The starting (0 m) and ending positions (12.56 m) referred to the same position at SL1 of the ring track. The adhesion coefficient was calculated by dividing the tangential force by the vertical (normal) force:

$$\mu = \sqrt{F_x^2 + F_y^2} \Big/ F_z \tag{1}$$

where μ is the adhesion coefficient, and F_x, F_y, and F_z are the contact forces in the longitudinal, lateral, and vertical directions, respectively.

Fig. 3a shows that the longitudinal force of W1 fluctuates around 200 N, and that of W3 changes between − 220 N and − 1200 N with an average value of − 575 N. W1 was in traction in most positions, while W3 was in braking conditions. The longitudinal forces were determined by the torques on W1 and W3 applied through a coupled gearbox [22]. We can only control the overall torque applied to the gearbox in the current setup but cannot control how the gearbox distributes the torque to the two wheels. The difference in the longitudinal force of W1 and W3 was caused by the uneven distribution of the wheel torque by the

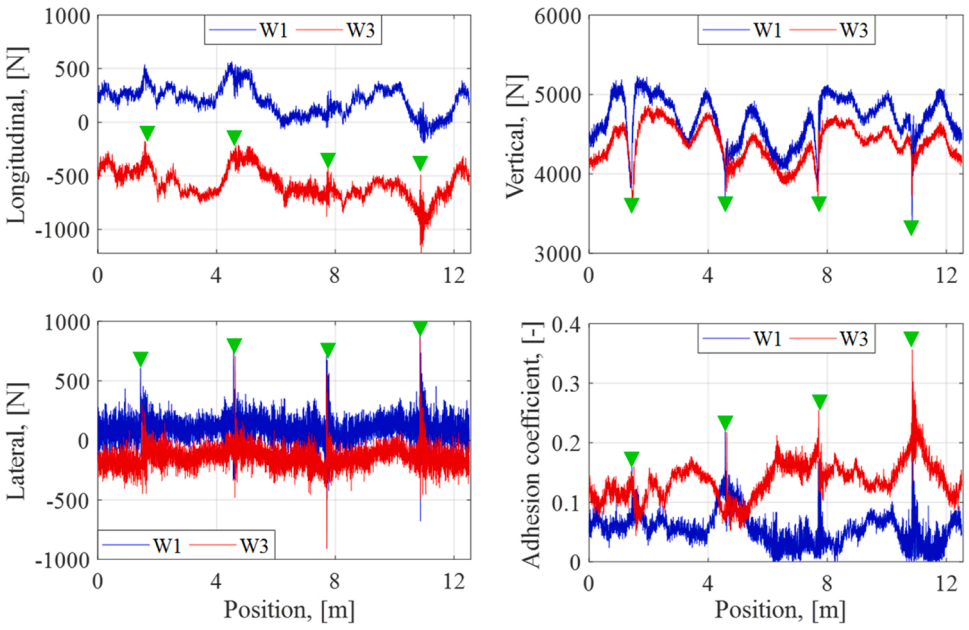

Fig. 3. Measured wheel-rail contact forces and adhesion coefficient of W1 and W3. (a) Longitudinal forces; (b) vertical forces; (c) lateral forces; (d) adhesion coefficient. The joint positions are marked by (▼).

gearbox. It can be seen from Fig. 3b that the measured vertical forces of W1 and W3 change mostly in the range of 4 kN and 5 kN. The vertical track irregularity causes this strong long-wavelength (i.e., 1–2 m) fluctuation. More efforts will be made to adjust the irregularity to achieve more even vertical force along the track in future work. The average vertical load of W1 is approximately 4650 N, slightly larger than of W3, which is 4400 N. Compared to the longitudinal and vertical forces, the overall lateral forces of both wheels are small, with average values of 100 N and − 140 N for W1 and W3, respectively, as shown in Fig. 3c. Besides, the impacts of the lateral forces at rail joints, corresponding to four dominant peaks in Fig. 3c (indicated by ▼), are significantly strong, which possibly result from the sudden change of the AoA at the joints where fishplates were absent. Fig. 3d depicts the adhesion coefficient of the two wheels. Neglecting the proximity to the joints, the adhesion coefficients of W1 and W3 are in the range of 0–0.1 and 0.1–0.2, respectively. Overall, the contact forces of the two wheels roughly satisfy the designed loading conditions to simulate the vehicle-track interaction on the field tangent track. Further better control of AoA and reduction of lateral contact force will be conducted in future work. In addition, the fluctuation of the wheel-rail contact forces allows us to study the influences of different axle loads, adhesion coefficients, and AoAs on corrugation formation.

2.2.2. *Corrugation measurement by the 3D HandyScan test*

After reproducing corrugation, the rail profile with corrugation was measured with a laser-based HandyScan, as shown in Fig. 4. In this measurement, the laser strips projected a reference on the rail surface, and two cameras captured the reflection signals and transmitted them to a data acquisition system (see Fig. 4a). When moving along the rail, the HandyScan positioned itself to a unique dynamic referencing system which ensured high measurement repeatability and accuracy. Fig. 4b shows an example of the measured corrugation in the V-Track in Fig. 1b. The longitudinal-vertical profile in the center of the running band was derived, and 15-point smooth was used to reduce the data noise. It can be seen that the corrugation wavelength is approximately 30 mm, agreeing well with the observation in Fig. 1b.

2.2.3. *Hardness test*

It has been reported in the literature that the rail hardness is varied along the corrugation because of the different microstructures at the peaks and troughs [26,27]. The hardness test was performed on the running band of the rail to capture the hardness variation along the corrugation, as shown in Fig. 5. A hardness tester (DynMIC34248) was used together with a self-developed ruler guide. The interval between two adjacent test points was 2 mm.

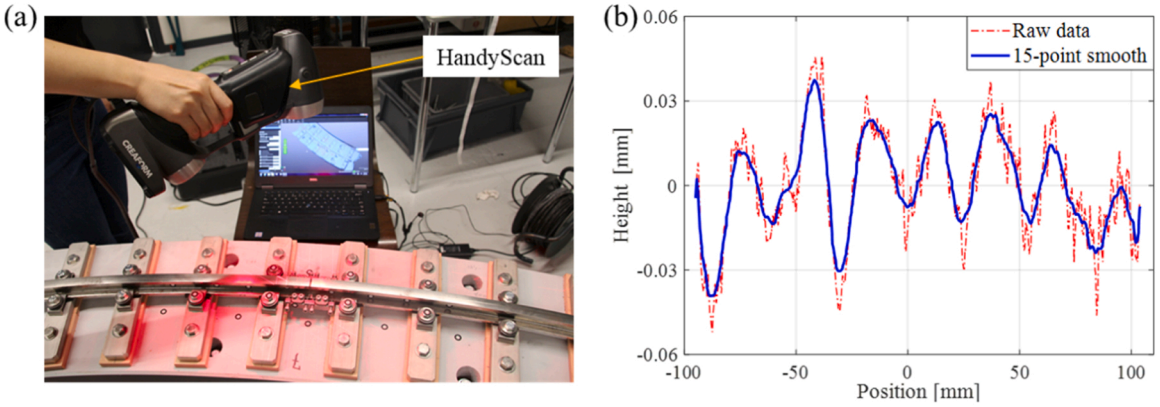

Fig. 4. Corrugation measurement by the 3D HandyScan test. (a) 3D HandyScan test; (b) measured corrugation in the V-Track in Fig. 1b.

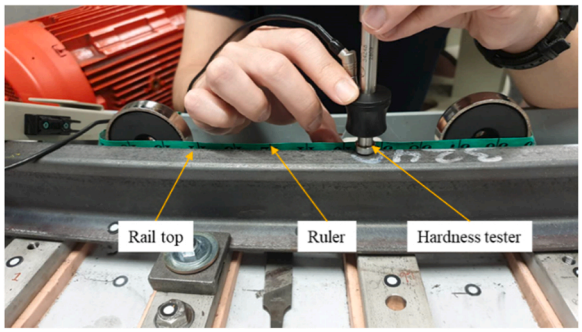

Fig. 5. Experimental setup for the hardness test in the V-Track.

The hardness values of the rails and the wheels were measured before the experiments to define their initial conditions. The hardness value of the original S7 rail is about 170 HB, lower than the field real rail (i.e., R260MN), which may influence the corrugation growth rate. After some trial running tests, the rail hardness has increased to about 210 HB. The wheel hardness increased from about 200 HB to 250 HB, which is harder than the rail.

2.2.4. *Hammer test*

Track dynamics is important to understand the wavelength-fixing mechanism of corrugation. Hammer test is a widespread testing technique to obtain the dynamic behavior of the railway tracks [28–30]. Fig. 6 shows the experimental setup for the hammer test in the V-Track. Two 3D accelerometers (PCB 356B21) were glued on the rail gauge face to capture the rail vibration signals. They were not placed on the rail head to avoid the contamination of the glue on the wheel-rail contact surfaces. One was on a rail section located above a sleeper (named 'on-support' in Fig. 6a), the other was in the middle of two sleepers (named 'mid-span' in Fig. 6a). A small hammer (PCB 086C03) with a metal tip was used to excite the rail in the high-frequency range. The excitation positions were as close as possible to the accelerometers in three directions. The vertical and lateral hammer impacts were conducted on the rail head and gauge face, respectively. The longitudinal impacts were applied through a self-made clamp, as shown in Fig. 6b. The frequency response function (FRF) is calculated as follows [31].

$$\mathrm{FRF}(f) = \frac{S_{aF}(f)}{S_{FF}(f)(2\pi f)^2} \tag{2}$$

where $S_{aF}$is the cross-spectrum between the acceleration and force, and S_{FF} *is* the auto-spectrum of the force, and f is frequency.

3. The reproduced corrugation in the V-Track

After 4500 rotations, corrugation was first observed from SL80 to SL85 of the V-Track. Fig. 7 shows the corrugation between SL84 and SL85, with the shiny parts marked by red lines on the rail surfaces. The corrugation wavelength observed in this figure is 6–7 mm. The running band was close to the inner edge of the rail head because of the rail tilt during the installation process. Its width was about 4 mm, larger than the 3.2 mm calculated based on the Hertz theory due to the plastic deformation [32]. There is a rail joint between SL85 and SL86. Because of the insufficient length of the two adjacent rails, a small piece of rail was included in this joint. This imperfect joint was just after the corrugation in the space and thus not the direct initiator of corrugation. Fastening clamps were used only at SL80 and SL85, and it was observed that one of the fastening bolts at SL85 was loose during the corrugation experiment, as shown in Fig. 7a. Overall, the imperfect joint, the absent fastening clamps at SL81- SL84, and the loose fastening bolt at SL85 lead to relatively weak constraint to the rail and serve as the initial excitation to the wheel-rail system for corrugation formation.

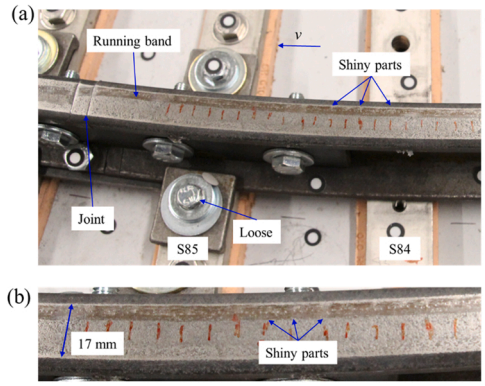

Fig. 7. The reproduced corrugation between SL84 and SL85 in the V-Track. (a) Corrugation with a wavelength of 6–7 mm in the V-Track; (b) close-up of the corrugation.

After observing the corrugation, we further run another 6000 rotations to grow the corrugation. Fig. 8 shows the measured corrugation in the spatial and wavelength domains after the 10,500 rotations from the 3D HandyScan test. The corrugation was between 10.72 m (middle of SL84 and S85) and 10.83 m (rail joint), just before the rail joint, which served as a reference point for the ease of comparison with the measurement results of the hardness and contact forces. It is observed from Fig. 8a that the corrugation amplitude (maximum peak to trough distance) is approximately 60 μm, indicating a relatively severely developed corrugation. Fig. 8b shows that the corrugation has two major wavelength components of 6.4 mm and 8.9 mm, respectively, and the wavelength of 6.4 mm is dominant with the highest PSD magnitude, which agrees with the observation in Fig. 7, where the wavelength is 6–7 mm. There are also some minor wavelength components, i.e., at 7.7 mm and 10.8 mm. According to the similarity law [23,24], the major corrugation wavelengths of 6.4 mm and 8.9 mm are approximately equivalent to 32 mm and 45 mm of corrugation wavelengths in the field

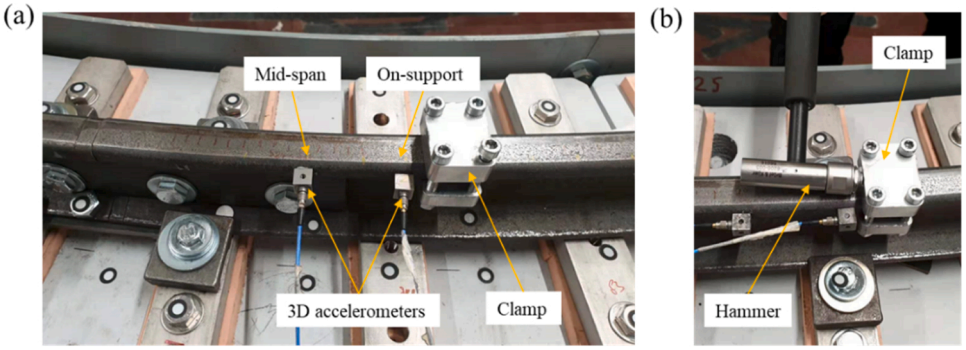

Fig. 6. Experimental setup for the hammer test in the V-Track. (a) Experimental setup; (b) longitudinal hammer excitation by a self-made clamp.

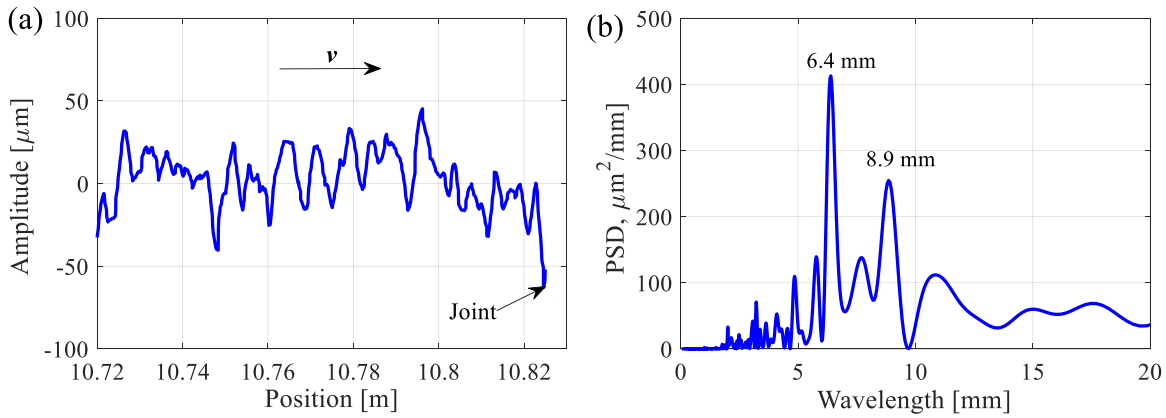

Fig. 8. The reproduced corrugation in the spatial and wavelength domains. (a) In the spatial domain, the corrugation just before the joint (at position 10.83 m) was selected for analysis; (b) in the wavelength domain.

considering a scale factor of 1/5. Therefore, the reproduced rail corrugation in the V-Track falls in the typical wavelength range of short pitch corrugation, and the analysis of its formation mechanism can be applied to understand the formation of corrugation in the field.

Fig. 9 shows measured rail hardness along the corrugation together with the rail profile. It can be seen that the rail hardness fluctuates between 195 HB and 235 HB and has a wave pattern similar to that of the rail profile. The hardness peaks correspond well to the corrugation peaks, as indicated by the dashed lines in Fig. 9, which agrees with the findings in [27], possibly resulting from different microstructures in the corrugation peaks and troughs due to the dynamic loads.

4. Corrugation development mechanism

In this section, the corrugation development mechanism is identified based on the measured wheel-rail contact forces, track dynamic behaviors a well as observations.

4.1. Corrugation wavelengths

The corrugation formation requires the continuous accumulation of differential wear or plastic deformation at certain locations, which means that wear or plastic deformation caused by one-wheel passage should repeat the same wavelength and phase as those of the previous wheel passages. The wheel-rail dynamic contact forces cause the wear and plastic deformation of the rails. It is thus inferred that the corrugation formation should depend on the repeatable wavelength and phase of the contact forces under multiple wheel passages. Fig. 10 and Fig. 11 show the measured contact forces with W1 and W3 at rotations 1 (beginning of the experiment), 5000 (middle) and 10,500 (end) in the spatial and wavelength domains, respectively.

Fig. 10a and Fig. 11a show that the overall longitudinal force with

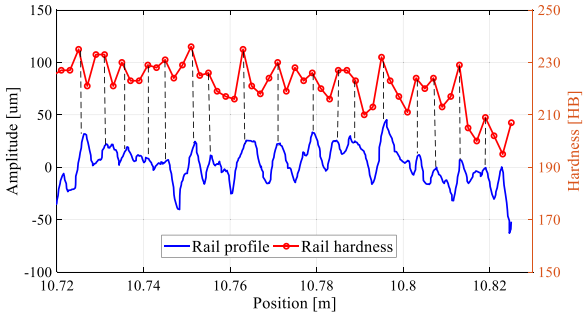

Fig. 9. Measured rail hardness along the corrugation compared with the rail profile.

W1 is small (below 100 N) with a wavelength of 7.7 mm, which may be related to a minor corrugation wavelength of 7.7 mm (see Fig. 8b). The vertical and lateral forces with W1 repeat the wavelength and phase for all the rotations, as shown in Figs. 10b and 10c. They both have a dominant wavelength component of 6.4 mm (see Figs. 11b, 11c), which should contribute to corrugation formation at 6.4 mm. It is found that the magnitude of the lateral force with W1 at 6.4 mm is considerably larger than that of the vertical force, indicating that the lateral force is dominant for the corrugation wavelength of 6.4 mm. It is also observed from Fig. 11c that the lateral force has another major wavelength component of 9.5 mm, which may be responsible for corrugation development at 8.9 mm. Fig. 11b shows that the vertical force with W1 has multiple wavelength components in 7–20 mm, and the one at 9.3 mm is the closest to the corrugation wavelength of 8.9 mm.

Fig. 10d shows that the longitudinal force with W3 fluctuates around − 850 N and repeats the wavelength and phase for all the rotations. It has a dominant wavelength component of 6.4 mm, as shown in Fig. 11d, which should be responsible for corrugation development at 6.4 mm. Fig. 10e and Fig. 11e depict that the vertical force with W3 also has repeatable wavelength and phase for all rotations with a major wavelength component of 6.7 mm, which is closely related to the corrugation wavelength of 6.4 mm. Due to the larger magnitude and closer to corrugation wavelength, the longitudinal force with W3 seems more decisive in corrugation development at 6.4 mm than the vertical force. Like W1, the vertical force with W3 also has multiple wavelength components in 7–20 mm, which may be relevant to some minor corrugation wavelengths. Among them, the wavelength of 8.6 mm is the closest to the corrugation wavelength of 8.9 mm. Fig. 11f shows the shift of major wavelength components of the lateral force with W3 from 7.4 mm at rotation 1, to 8.3 mm at rotation 5000, and to 9.0 mm at rotation 10,500, which leads to their phase difference at some positions in Fig. 10f, such as in 10.80–10.81 m. The wavelength components of 8.3 mm and 9.0 mm may contribute to the corrugation wavelength of 8.9 mm.

In summary, the lateral and vertical forces with W1 and the longitudinal and vertical forces with W3 together determine the corrugation development at the dominant wavelength component of 6.4 mm. Compared to the vertical forces, the tangential (frictional) force components that cause the differential wear, namely the lateral force with W1 and longitudinal force with W3 in this case, should play a major role in the corrugation formation. Further, it is found that the average magnitude of the W3 longitudinal force (−850 N) is significantly larger than that of the W1 lateral force (150 N) and thus much more decisive on the wear process of the rail surface. Therefore, it is concluded the longitudinal force of the W3-track system is dominant for corrugation development at 6.4 mm. Although there are no wavelength components of contact forces that exactly match the corrugation wavelength of

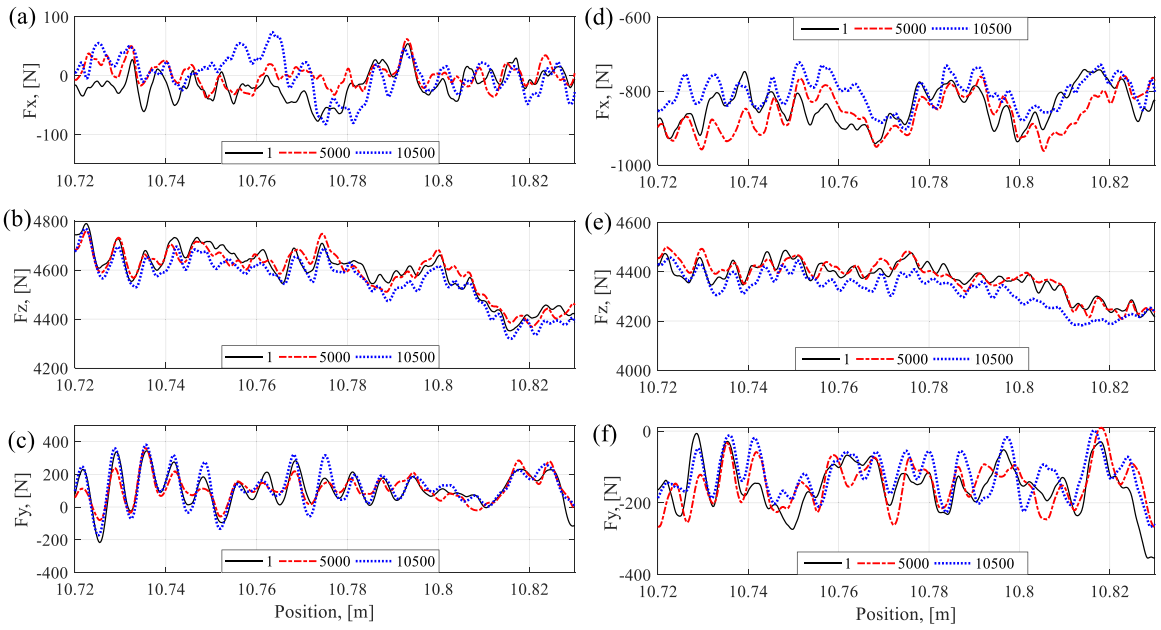

Fig. 10. Measured wheel-rail dynamic contact forces of W1 and W3 in the spatial domain at rotations 1, 5000 and 10,500. (a) Longitudinal force of W1; (b) vertical force of W1; (c) lateral force of W1; (d) longitudinal force of W3; (e) vertical force of W3; (f) lateral force of W3.

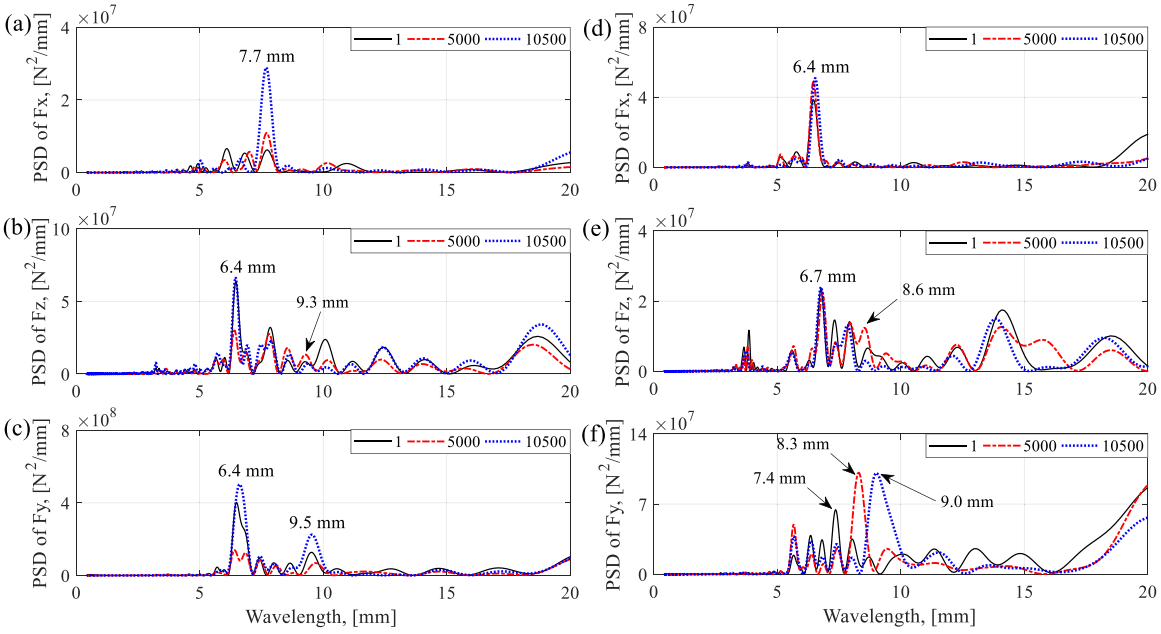

Fig. 11. Measured wheel-rail dynamic contact forces of W1 and W3 in the wavelength domain at rotations 1, 5000 and 10,500. (a) Longitudinal force of W1; (b) vertical force of W1; (c) lateral force of W1; (d) longitudinal force of W3;(e) vertical force of W3; (f) lateral force of W3.

8.9 mm, it is observed that the lateral force wavelength of 9.5 mm with W1, vertical force wavelength of 9.3 mm with W1, lateral force wavelengths of 8.3 mm and 9.0 mm with W3, vertical force wavelength of 8.6 mm with W3 are quite close to it. It is thus inferred that the modulation of these wavelength components contributes to the corrugation development at 8.9 mm. The other wavelength components of contact forces (i.e., between 7 and 20 mm) may be related to some minor corrugation wavelengths. In addition, the repetitive wavelength and phase of the contact forces confirm that corrugation consistently grows at certain locations of the rail.

4.2. *Corrugation frequencies*

The characteristic frequency f is the quotient of the running speed v and a characteristic wavelength λ, as follows.

$$f = \frac{v}{\lambda} \tag{3}$$

With the running speed of 13 km/h, the two corrugation characteristic frequencies are calculated as 564 Hz and 405 Hz, corresponding to the wavelength components of 6.4 mm and 8.9 mm (see Fig. 8b). This equation also applies to the calculation of characteristic frequencies of the wheel-rail contact forces.

Grassie [33] reported that all types of corrugation that have been

documented to date are essentially constant-frequency phenomena, which are determined by the eigen frequencies of the vehicle-track system. Track dynamic behaviors characterized by FRFs were obtained by the hammer test to identify the corrugation frequencies. Figs. 12a, b, c show the measured FRFs in the longitudinal, vertical, and lateral directions, respectively, with the excitations of on-support and mid-span. Some resonance peaks and anti-resonance dips are observed in the FRFs with strong fluctuation amplitudes, corresponding to different rail vibration modes [34,35]. It is found that the corrugation frequency of 564 Hz corresponds well to a longitudinal anti-resonance mode at 574 Hz, a vertical resonance mode at 570 Hz, and a lateral resonance mode at 572 Hz (indicated by arrows in Fig. 12). The corrugation frequency of 405 Hz corresponds to a vertical and a lateral resonance mode at 400 Hz (indicated by arrows in Figs. 12b and 12c), while no relevant longitudinal mode is found in Fig. 12a.

4.3. Corrugation development mechanism

To better understand the corrugation development mechanism, the characteristic wavelengths and frequencies of the corrugation, contact forces, and relevant rail vibration modes are summarized in Table 2. The numbers are colored depending on their relevance to the corrugation wavelengths and frequencies. Those related to corrugation wavelength of 6.4 mm or frequency of 564 Hz are set to be blue. Numbers related to corrugation wavelength of 8.9 mm or frequency of 405 Hz are set to be orange. Other numbers are set to be black.

A general process for corrugation development is identified based on observations and measurement results of wheel-rail dynamic contact forces and track dynamic behaviors. First, the imperfect joint, the absent fastening clamps at SL81- SL84, and the loose fastening bolt at SL85 are identified as the initial excitation to the V-Track vehicle-track system, which leads to a weaker constraint to the rail. Hence some rail vibration modes cannot be effectively suppressed, as shown in Fig. 12 and Table 2. Afterward, when the wheel rolls over the rail, these vibration modes are excited and induce wheel-rail dynamic contact forces with a certain wavelength and phase. With multiple wheel passages, the dynamic contact forces repeat the same wavelength and phase as the previous ones, as shown in Fig. 10. During this process, the differential wear or plastic deformation caused by the dynamic contact forces continuously accumulates at certain rail locations. Corrugation can thus consistently initiate and grow.

5. Discussions

5.1. Validation and extension of the new insights in [6,15]

Li et al. [6,15] numerically studied the development mechanism of short pitch corrugation employing a validated 3D FE vehicle-track interaction model [36–38] and indicated that rail longitudinal vibration modes are responsible for corrugation initiation. This insight agrees with the experimental results of the W3-track system that the longitudinal rail mode at 574 Hz contributes to corrugation development at 6.4 mm. The simulation results further inferred that the frequencies of five dynamic quantities, longitudinal contact force, vertical contact force, longitudinal vibration mode, vertical vibration mode, and differential wear, may converge to one frequency, corrugation characteristic frequency that corrugation can consistently initiate and grow. The corrugation experiment in this paper agrees with the findings of [6].

In addition, the experimental results of the W1-track system show that the rail lateral vibration mode can also dominate corrugation development. In the FE simulation of [6,15], lateral vibration modes and lateral force were not analyzed because the lateral wheel-rail interaction

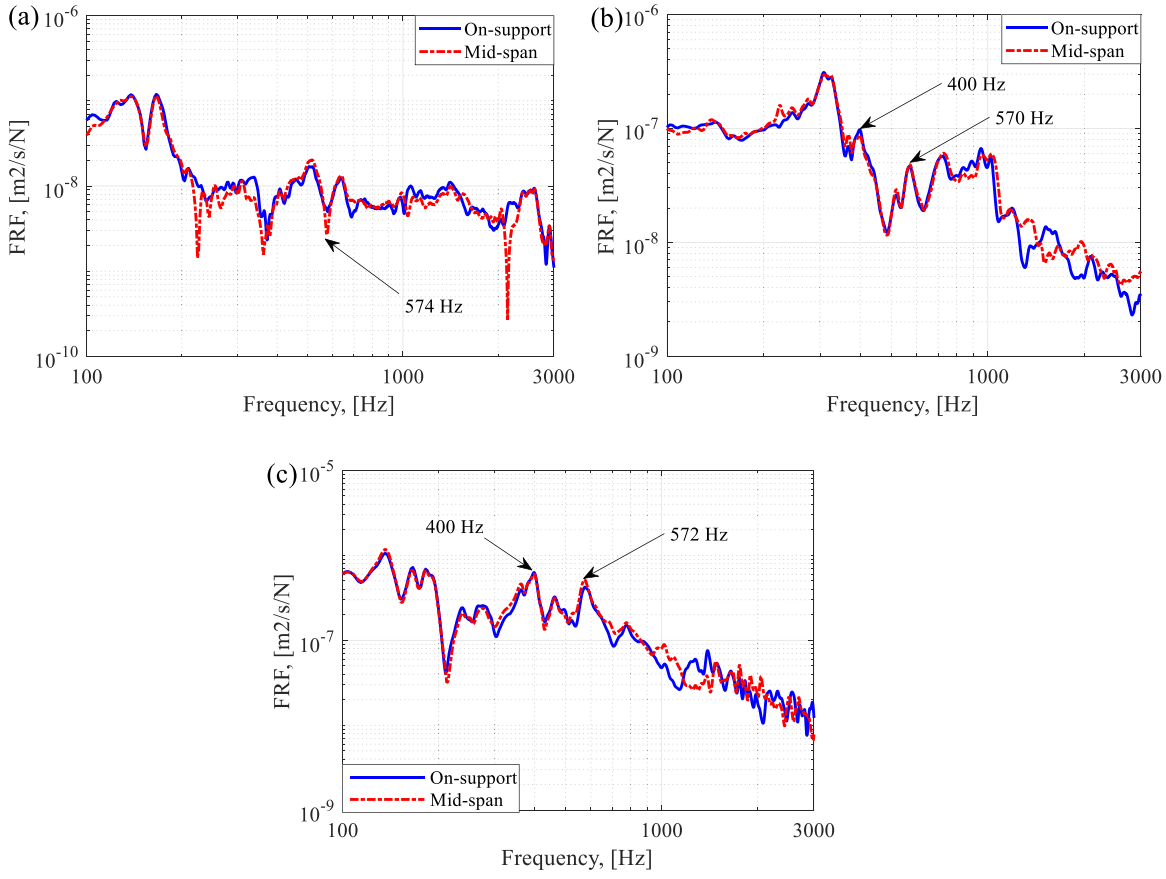

Fig. 12. Measured FRFs in three directions with the on-support and the mid-span excitations. (a) Longitudinal FRF; (b) vertical FRF; (c) lateral FRF.

Table 2
Characteristic wavelengths and frequencies of corrugation, contact forces, and relevant track vibration modes. The numbers are colored depending on their relevance to the corrugation wavelengths and frequencies (in boldface). The numbers related to the corrugation wavelength of 6.4 mm or frequency of 564 Hz are set to be blue. The numbers related to the corrugation wavelength of 8.9 mm or frequency of 405 Hz are set to be orange. Otherwise, they are set to be black.

Dynamic quantities	W1-track system		W3-track system	
	Wavelength (mm)	Frequency (Hz)	Wavelength (mm)	Frequency (Hz)
Corrugation	**6.4** **8.9**	**564** **405**	**6.4** **8.9**	**564** **405**
Longitudinal contact force	7.7	469	6.4	564
Vertical contact force	6.4 9.3	564 388	6.7 8.6	540 420
Lateral contact force	6.4 9.5	564 381	7.4 8.3 9.0	488 435 401
Longitudinal vibration mode, Hz	574			
Vertical vibration mode, Hz	400, 570			
Lateral vibration mode, Hz	400, 572			

is generally considered weak on tangent tracks and hence negligible to corrugation formation. Nevertheless, Fig. 10c shows that the fluctuation amplitude of the lateral force can be considerably large despite a small AoA. That is possible because the track has the largest flexibility in the lateral direction compared to those in the longitudinal and vertical directions, as shown in Fig. 12, and with the same excitation, the lateral vibration is the strongest. Therefore, in the field railways, with a small yaw angle and initial excitation, lateral track vibration modes could be excited and contribute to the formation of corrugation.

Overall, the new insights in [6,15] about longitudinal vibration modes and the consistency condition for corrugation development have been validated by the experimental results. This paper provides the first experimental evidence to the best knowledge of the authors, indicating that rail longitudinal vibration modes contribute to the consistent development of short pitch corrugation.

5.2. *Vertical vibration modes are not decisive to corrugation formation*

A widely accepted hypothesis in the literature is that vertical vibration modes induce the varying vertical (normal) force that determines the development of short pitch corrugation [3,4,9,39,40]. This hypothesis is probably based on the fact that the wheel-rail interaction mainly acts in the vertical direction. The longitudinal and lateral vibration modes have not been included in most analytical and numerical studies in the literature. Except for the unawareness of their significance, another possible reason is the limitation of the previous models that cannot directly and instantaneously consider the coupling of 3D structural dynamics and the contact mechanics of the vehicle-track system. For the corrugation simulation, the tangential force in these models is usually assumed to be constant [39] or fluctuate depending on the normal force [40]. Nevertheless, the experimental results in this paper indicate that the fluctuation of tangential force is independent of but much larger than that of the vertical force. This fluctuation is mainly determined by the longitudinal and lateral vibration modes excited from the vehicle-track dynamic interaction. Although the vertical vibration modes and vertical dynamic forces play a role in the corrugation formation, they seem not as decisive as those in the longitudinal and lateral directions.

5.3. *The initial excitation is necessary for corrugation development*

Corrugation is not observed everywhere on the track but at some particular locations. Hence, it is reasonable to assume that the track that can develop corrugation has some initial energy input to excite the vehicle-track system called 'initial excitation' [15]. With the initial excitation, rail vibration modes are excited and induce dynamic wheel-rail contact forces. These dynamic forces result in differential wear or plastic deformation that is responsible for corrugation development. In some situations, the initial excitation of corrugation is obvious, for instance, the joint-, the scratch-, and the squat-induced corrugation [1,23,41–43], which follows the excitation and often decays out over a finite number of wavelengths. In other situations, the initial excitation seems invisible (i.e., railpad aging), and the corrugation can develop over a much longer distance.

The purpose of this work is to reproduce the latter corrugation. Therefore, fastening clamps were installed only every three or four sleepers to simulate the fastening degradation in the field, which may provide a potentially preferred condition for corrugation initiation and growth. The loose fastening bolt at SL85 was unexpected and observed during the corrugation experiment. Four rail joints were used to connect the four rails, and only the joint between SL85 and SL86 used a small piece of rail because of the insufficient length of the adjacent rails. The absent fastening clamps at SL81- SL84, the loose fastening bolt at SL85, and the imperfect joint, together serve as the initial excitation for the corrugation development that is at SL80-SL85. The latter two factors probably play a more important role because corrugation was not observed in the vicinity of the other three joints.

5.4. *The loading conditions may influence the excited rail vibration modes and corrugation formation mechanism*

The previous analysis indicates that W1 and W3 excited different rail vibration modes as the wavelength-fixing mechanisms of corrugation. It is noted from Fig. 10 that the initial loading conditions of W1 and W3 are quite different. For instance, the quasi-static longitudinal load of W3 is around − 850 N while that of W1 is around 0 N. W3 excited the longitudinal vibration mode at 574 Hz while W1 did not, indicating the stronger interaction and coupling is more likely to excite the

corresponding vibration modes. The quasi-static lateral forces of both wheels are around 100–140 N but in different directions. W1 excited the lateral vibration mode at 572 Hz while W3 did not, suggesting that the loading direction could influence the excited vibration modes considering the asymmetrical position of running banding on the rail head. Overall, these experiment results indicate that the values and directions of the initial loadings of the vehicle-track system may influence the excited rail vibration modes, and thus the wavelength-fixing mechanism of corrugation.

6. Conclusions and future work

In this paper, an experimental study of short pitch corrugation has been performed using the V-Track test rig. The employed V-Track configuration consists of two wheel assemblies (W1 and W3) and a ring track and can simulate the high-frequency dynamics of the real vehicle-track system, which is crucial to understanding the wavelength-fixing mechanism of short pitch corrugation. The loading conditions of the V-Track were first designed and adjusted by the wheel preload springs, the braking torque, and the angle of attack to simulate the vehicle-track interactions. Short pitch corrugation was successfully reproduced between SL80 and SL85 of the V-Track, and its spatial distribution, wavelength components, and hardness variation were captured by the 3D HandyScan and the hardness tests. Based on the measurement results of wheel-rail contact forces and track dynamic behaviors and observations, the development mechanism of short pitch corrugation was identified. The main conclusions are summarized as follows.

1. The reproduced rail corrugation in the V-Track has two major wavelengths of 6.4 mm and 8.9 mm, and the wavelength of 6.4 mm is dominant with the higher PSD magnitude. They are approximately equivalent to 32 mm and 45 mm of corrugation wavelengths in the field considering a scale factor of 1/5, falling in the typical short pitch range. Therefore, the study of its formation mechanism can be applied to understand short pitch corrugation in the field.
2. The process for the consistent development of the short pitch corrugation is identified. The imperfect joint, the loose fastening bolt at SL85, and the absent fastening clamps at SL81- SL84 together serve as the initial excitation to the V-Track vehicle-track system, which leads to a weaker constraint to the rail. Hence some rail vibration modes cannot be effectively suppressed and induce dynamic wheel-rail contact forces with a certain wavelength and phase when the wheel rolls over the rail. With multiple wheel passages, the dynamic contact forces repeat the same wavelength and phase as the previous ones, and the resulting differential wear or plastic deformation can continuously accumulate at certain locations of the rail, causing consistent corrugation growth.
3. Specifically, two types of wavelength-fixing mechanisms of short pitch corrugation at 6.4 mm are identified for the two wheel-track systems with W1 and W3. For the W1-track system, the rail lateral vibration mode at 572 Hz and vertical mode at 570 Hz, and the induced vertical and lateral contact forces at 564 Hz contribute to the corrugation development at 6.4 mm. For the W3-track system, the longitudinal mode at 574 Hz and the induced longitudinal force at 564 Hz together with the vertical mode at 570 Hz and the vertical force at 540 Hz are responsible for the corrugation wavelength of 6.4 mm. Among these quantities, the longitudinal vibration mode and the induced longitudinal force of the W3-track system play a dominant role.
4. For both wheel-track systems, the lateral and vertical modes at 400 Hz and the induced lateral and vertical dynamic contact forces determine the corrugation development at 8.9 mm.
5. The experimental results validated the hypotheses in [6] about longitudinal vibration modes and the consistency condition for short pitch corrugation development. To the best knowledge of the authors, this paper provides the first experimental evidence which indicates that rail longitudinal vibration mode contributes to the consistent development of short pitch corrugation.
6. The experimental results in this work indicate that although they play a role in the corrugation formation, the vertical vibration modes and the induced vertical dynamic contact forces are not as decisive and dominant as those in the longitudinal and lateral directions.
7. The initial loading conditions of the vehicle-track system may influence the excited rail vibration modes and thus the wavelength-fixing mechanism of short pitch corrugation.

The experimental results and findings can be applied to understand the development mechanism of short pitch corrugation in the field. In future work, the softer S7 rails will be replaced with scaled 1/5 rails cutting from the real rails to more realistically simulate the field wheel-rail dynamic contact. Further metallurgical investigation of rail in the presence of corrugation will be performed to understand the corrugation damage mechanism and explain the measured hardness variation along the corrugation. Besides, mitigation approaches for short pitch corrugation will be designed and validated using the V-Track test rig in future work.

Statement of originality

1) The paper has not been published previously, that it is not under consideration for publication elsewhere, and that if accepted it will not be published elsewhere in the same form, in English or in any other language, without the written consent of the publisher. 2) The paper does not contain material which has been published previously, by the current authors or by others, of which the source is not explicitly cited in the paper.

Declaration of Competing Interest

The authors declare that they have no known competing financial interests or personal relationships that could have appeared to influence the work reported in this paper.

Data availability

Data will be made available on request.

Acknowledgements

The authors thank Jan Moraal for performing the V-Track tests and acquiring the data. The authors thank Julian He, Yang Jin, and Siwarak Unsiwilai for helping with the 3D HandyScan test, hammer test, and hardness test. The first author thanks the China Scholarship Council (201607000026) for the support.

References

[1] Grassie SL, Kalousek J. Rail corrugation: characteristics, causes and treatments. proceedings of the institution of mechanical engineers. Part F J Rail Rapid Transit 1993;207:57–68.
[2] Grassie SL, Johnson KL. Periodic microslip between a rolling wheel and a corrugated rail. Wear 1985;101:291–309.
[3] Hempelmann K, Knothe K. An extended linear model for the prediction of short pitch corrugation. Wear 1996;191:161–9.
[4] Hiensch M, Nielsen JCO, Verheijen E. Rail corrugation in The Netherlands—measurements and simulations. Wear 2002;253:140–9.
[5] Igeland A, Ilias H. Rail head corrugation growth predictions based on non-linear high frequency vehicle/track interaction. Wear 1997;213:90–7.
[6] Li S, Li Z, Núñez A, Dollevoet R. New Insights into the short pitch corrugation enigma based on 3d-fe coupled dynamic vehicle-track modeling of frictional rolling contact. Appl Sci 2017:7.
[7] Muller S. A linear wheel-track model to predict instability and short pitch corrugation. J Sound Vib 1999;227:899–913.
[8] Nielsen JB. Evolution of rail corrugation predicted with a non-linear wear model. J Sound Vib 1999;227:915–33.

[9] Wu TX, Thompson DJ. An investigation into rail corrugation due to micro-slip under multiple wheel/rail interactions. Wear 2005;258:1115–25.
[10] Knothe K, Groß-Thebing A. Short wavelength rail corrugation and non-steady-state contact mechanics. Veh Syst Dyn 2008;46:49–66.
[11] Wu B, Wang W, Pan J, Hu Y, Xu R, Ye D, et al. Study on corrugated wear on high-speed railways based on an improved finite element model of wheel-rail rolling contact. Tribol Int 2022:108199.
[12] Oostermeijer KH. Review on short pitch rail corrugation studies. Wear 2008;265:1231–7.
[13] Grassie SL. Rail corrugation: advances in measurement, understanding and treatment. Wear 2005;258:1224–34.
[14] Böhmer A, Klimpel T. Plastic deformation of corrugated rails—a numerical approach using material data of rail steel. Wear 2002;253:150–61.
[15] Li Z, Li S, Zhang P, Núñez A, Dollevoet R. Mechanism of short pitch rail corrugation: initial excitation and frequency selection for consistent initiation and growth. Int J Rail Transp 2022:1–36.
[16] Zhang P, Li S, Li Z. Short pitch corrugation mitigation by rail constraint design. Int J Mech Sci 2022:108037.
[17] Bellette PA, Meehan PA, Daniel WJT. Validation of a tangent track corrugation model with a two disk test rig. Wear 2011;271:268–77.
[18] Matsumoto A, Sato Y, Ono H, Tanimoto M, Oka Y, Miyauchi E. Formation mechanism and countermeasures of rail corrugation on curved track. Wear 2002;253:178–84.
[19] Jin X, Wen Z. Rail corrugation formation studied with a full-scale test facility and numerical analysis. Proc Inst Mech Eng, Part J J Eng Tribology 2007;221:675–98.
[20] Saulot A, Descartes S, Berthier Y. Sharp curved track corrugation: from corrugation observed on-site, to corrugation reproduced on simulators. Tribol Int 2009;42:1691–705.
[21] Suda Y, Komine H, Iwasa T, Terumichi Y. Experimental study on mechanism of rail corrugation using corrugation simulator. Wear 2002;253:162–71.
[22] Zhang P, Moraal J, Li ZL. Design, calibration and validation of a wheel-rail contact force measurement system in V-Track. Measurement 2021:175.
[23] Naeimi M, Li Z, Petrov RH, Sietsma J, Dollevoet R. Development of a new downscale setup for wheel-rail contact experiments under impact loading conditions. Exp Tech 2017;42:1–17.
[24] Jaschinski A, Chollet H, Iwnicki S, Wickens A, Würzen J. The application of roller rigs to railway vehicle dynamics. Veh Syst Dyn 1999;31:345–92.
[25] Yang Z, Zhang P, Moraal J, Li Z. An experimental study on the effects of friction modifiers on wheel–rail dynamic interactions with various angles of attack. Railw Eng Sci 2022;30:360–82.
[26] Feller HG, Walf K. Surface-analysis of corrugated rail treads. Wear 1991;144:153–61.
[27] Wild E, Wang L, Hasse B, Wroblewski T, Goerigk G, Pyzalla A. Microstructure alterations at the surface of a heavily corrugated rail with strong ripple formation. Wear 2003;254:876–83.
[28] Oregui M, Li Z, Dollevoet R. Identification of characteristic frequencies of damaged railway tracks using field hammer test measurements. Mech Syst Signal Process 2015;54–55:224–42.
[29] Yang Z, Boogaard A, Chen R, Dollevoet R, Li ZL. Numerical and experimental study of wheel-rail impact vibration and noise generated at an insulated rail joint. Int J Impact Eng 2018;113:29–39.
[30] Fourie D, Fröhling R, Heyns S. Railhead corrugation resulting from mode-coupling instability in the presence of veering modes. Tribol Int 2020:152.
[31] Maia NMM, e Silva JMM. Theoretical and experimental modal analysis. Research Studies Press; 1997.
[32] Zhao X, Li ZL. A three-dimensional finite element solution of frictional wheel-rail rolling contact in elasto-plasticity. Proc I Mech Eng J-J Eng 2015;229:86–100.
[33] Grassie SL. Rail corrugation: characteristics, causes, and treatments. P I Mech Eng F-J Rail 2009;223:581–96.
[34] Zhang P, Li S, Núñez A, Li Z. Vibration modes and wave propagation of the rail under fastening constraint. Mech Syst Signal Process 2021:160.
[35] Zhang P, Li SG, Nunez A, Li ZL. Multimodal dispersive waves in a free rail: numerical modeling and experimental investigation. Mech Syst Signal Process 2021:150.
[36] Molodova M, Li Z, Núñez A, Dollevoet R. Validation of a finite element model for axle box acceleration at squats in the high frequency range. Comput Struct 2014;141:84–93.
[37] Naeimi M, Li S, Li Z, Wu J, Petrov RH, Sietsma J, et al. Thermomechanical analysis of the wheel-rail contact using a coupled modelling procedure. Tribol Int 2018;117:250–60.
[38] Yang Z, Deng X, Li Z. Numerical modeling of dynamic frictional rolling contact with an explicit finite element method. Tribol Int 2019;129:214–31.
[39] Grassie SL, Edwards JW. Development of corrugation as a result of varying normal load. Wear 2008;265:1150–5.
[40] Ilias H. The influence of railpad stiffness on wheelset/track interaction and corrugation growth. J Sound Vib 1999;227:935–48.
[41] Li Z, Dollevoet R, Molodova M, Zhao X. Squat growth—some observations and the validation of numerical predictions. Wear 2011;271:148–57.
[42] Deng X, Qian Z, Li Z, Dollevoet R. Investigation of the formation of corrugation-induced rail squats based on extensive field monitoring. Int J Fatigue 2018;112:94–105.
[43] Jin X, Wen Z, Wang K, Zhang W. Effect of a scratch on curved rail on initiation and evolution of rail corrugation. Tribol Int 2004;37:385–94.